Nanoscale Horizons

ROYAL SOCIETY OF CHEMISTRY

COMMUNICATION

View Article Online
View Journal | View Issue

Cite this: *Nanoscale Horiz.*, 2026, **11**, 1345

Received 16th December 2025,
Accepted 22nd January 2026

DOI: 10.1039/d5nh00817d

rsc.li/nanoscale-horizons

Growing bright: ligand-controlled growth of aqueous colloidal Cu–In–Zn–S nanocrystals

Caterina Bellatreccia,[a] Angelica Germinario,[a] Zakaria Ziani, †[a] Alessandro Gradone,[b] Sirous Khabbaz Abkenar, [c] Giorgio Divitini, [c] Marco Villa *[a] and Paola Ceroni *[a]

To broaden the potential applications of colloidal quantum dots, sustainable synthetic protocols must be developed and optimised. In this report, we use a low-temperature water-based synthesis of Cu–In–Zn–S quantum dots (CIZS) and we analyse the effect of different ligands (citrate, ascorbate, glutathione, cysteine and mercapto-acetic acid) on crystal growth and composition. The ligands employed have a strong effect on the metal incorporation within the nanocrystal, leading to wide tunability of the photophysical behaviour of the resulting CIZS quantum dots.

New concepts

This work presents the low-temperature aqueous synthesis of alloyed Cu–In–Zn–S (CIZS) quantum dots (QDs) with a graded composition, highlighting the pivotal role of ligands in directing nanocrystal composition and tuning their optical properties. Unlike conventional synthetic approaches that rely on high temperatures and organic solvents – limiting biocompatibility and sustainability – our method operates in aqueous solution under mild conditions, offering a greener alternative. We demonstrate that thiolated ligands, such as glutathione, cysteine, and mercaptoacetic acid, are essential to obtain CIZS QDs with high photoluminescence quantum yield (~20%) and excellent colloidal stability in water. In contrast, non-thiolated ligands, like alanine, lead to poorly emissive and unstable nanocrystals. The ligand identity not only affects surface passivation but also dictates emission energy by modulating the Cu : In : Zn molar ratio upon modulation of binding strength. For example, mercaptoacetic acid favours the growth of stoichiometric nanocrystals with a Cu : In ratio of 1 : 1; the use of ascorbate instead of citrate lowers the amount of Zn^{2+} incorporated. These findings provide an alternative approach to tune the photophysical, optical, and colloidal properties of water-based CIZS QDs, whose growth is otherwise difficult to control, offering a pathway toward their biocompatible and sustainable application while advancing the understanding of Cu–In–Zn–S nanocrystals.

Introduction

In the last few decades, quantum dots (QDs) have emerged with outstanding optical properties that have paved the way for applications not only in lighting devices,[1,2] but also in bioimaging.[3–7] Unlike conventional organic fluorophores, QDs exhibit high photostability, high absorption coefficients, tunable emission from visible to NIR and high photoluminescence quantum yield (PLQY).[8–11] Moreover, passivating ligands can be tailored for specific targeting or multifunctionality, making QDs ideal candidates for biomedical purposes.[12–14]

Classical IV–VI, II–VI and III–V QDs contain heavy metal ions like Cd(II), Pb(II) or As(III) and pose significant toxicity concerns.[15–18] Consequently, there is a growing demand for QDs that are inherently less toxic and more biocompatible. Among the alternatives, I–III–VI QDs like copper indium sulfide ($CuInS_2$, CIS) QDs have gained considerable attention due to their reduced toxicity.[19–22] Like other QDs, the ternary I–III–VI QDs also show high molar absorption coefficients, size- and composition-dependent emission color, which extends into the red and near-infrared (NIR) spectral regions, and long photoluminescence lifetimes (hundreds of ns).[23–25] These features make $CuInS_2$ quantum dots particularly well-suited for tissue imaging, as they emit in spectral and time windows where biological tissues exhibit minimal autofluorescence and light scattering, enabling optical imaging with enhanced contrast and spatial resolution.[8,26] Importantly, CIS nanocrystals display a remarkable tolerance toward intrinsic defects, which not only contributes to their emission properties, but also broadens the range of possible synthetic modifications by doping with other metal ions.[27–30]

The most conventional synthetic routes for QDs employ high temperatures and organic solvents, hindering their use in the afore-mentioned fields for biocompatibility and sustainability reasons. Low-temperature routes for the synthesis of quantum dots in water have been developed for addressing this issue,[31–33]

[a] *Dipartimento di Chimica "Giacomo Ciamician" Alma Mater Studiorum – Università di Bologna, Via Gobetti 85, Bologna 40129, Italy. E-mail: marco.villa11@unibo.it, paola.ceroni@unibo.it*
[b] *Istituto per lo Studio dei Materiali Nanostrutturati (ISMN) - CNR Sede di Bologna, via Gobetti 101, Bologna 40129, Italy*
[c] *Istituto Italiano di Tecnologia, via Morego 30, Genoa 16163, Italy*
† Current address: Université Paris Cité, CNRS, ITODYS, F-75013 Paris, France.

but a detailed analysis of the role of each reagent in the synthesis and a deep understanding of the growth mechanism in these procedures is still lacking. In particular, ligands play a crucial role in QD synthesis and the resulting QD optical properties: from controlling nucleation and growth during synthesis to modulating surface states that directly affect optical properties, colloidal stability, and biocompatibility.[34–36] Several studies have shown that changes in the passivating ligand drastically alter the emission wavelength, photoluminescence lifetime and PLQY. In alloyed or doped CIS systems – such as Cu–In–Zn–S – the choice of ligand can determine dopant incorporation extent or shell growth behaviour (*e.g.*, ZnS), drastically affecting the photophysical properties of the resulting QDs.[37–40]

In this context, understanding the role of the ligand in the growth and composition of Cu–In–Zn–S (CIZS) quantum dots is essential for optimizing their photophysical properties and the synthetic protocol. In the present work, we tested two families of water-soluble ligands **L1** and **L2** (Fig. 1) in the synthesis of CIZS quantum dots in water: two O-based hard ligands (ascorbate **ASC**, citrate **CIT**) and three ligands containing soft S-based groups (mercaptoacetic acid **MAA**, glutathione **GSH**, cysteine **CYS**). We correlated the photophysical properties of the resulting quantum dots to their composition, and we studied the growth and composition of the quantum dots with *in situ* spectroscopy during synthesis.

Results and discussion

Synthesis and structural characterisation

CIZS@L1–L2 samples were prepared following a water-based, one-pot synthesis adapted from the literature (Fig. 1).[28,31] The metal precursor feeding molar ratio was kept constant (Cu : In : Zn = 1 : 3 : 18) and the amount of **L1** and **L2** ligands was adjusted to ensure good colloidal stability during the synthesis of all batches (see Experimental section for details). The injection of Na_2S initiates nucleation of **CIS@L1–L2** cores at 95 °C. After 40 minutes, the pH is adjusted to 6.5–7 and a solution of zinc(II) acetate, thiourea and ligand **L2** is added. The reaction mixture is kept at 95 °C for another 45 minutes to allow zinc(II) incorporation into the nanocrystals, yielding the corresponding **CIZS@L1–L2** samples.

It should be noted that non-thiolated **L2** ligands were tested (alanine, lysine, tyrosine, phenylalanine), but none of them yielded colloidally stable nanocrystals, indicating that the thiol functionality in the **L2** ligand is crucial for the stability of these quantum dots (see the SI).

All the synthesized batches show the characteristic XRD pattern of the zinc blend lattice, indicating that the different ligands do not change the preferred crystal structure of the quantum dots (Fig. S2). The size distribution of the samples was evaluated using high angle annular dark Field (HAADF) - scanning transmission electron microscopy (STEM) analyses. The average diameters, obtained by fitting the various distributions with Gaussian functions, are not significantly different within experimental error (Fig. S4–S6): all **CIZS@L1–L2** samples exhibit diameters in the range of 3–4 nm, with variable size distribution curves (Table 1, Fig. S6 and S7). EDX measurements carried out on two representative samples (**CIZS@CIT-GSH** and **CIZS@ASC-MAA**, Fig. S8 and S9) show that Cu, In, and Zn are localised in the same regions of the specimen, indicating that no significant phase segregation occurs during the synthesis. In addition to that, EDX mapping suggests that Cu and In are predominantly localized in the central regions of the nanoparticles, whereas Zn is distributed more uniformly over the entire particle volume. This distribution pattern suggests an alloyed structure with graded composition, in which the nanoparticles possess Cu/In-rich cores and Zn-rich outer layers.

The elemental composition was determined *via* atomic emission spectroscopy (MP-AES) for the different **CIZS@L1–L2** samples (Fig. 2). The molar ratio Cu : In : Zn can be extensively varied without affecting the zinc-blende crystal structure. The Cu : In molar ratio of the nanocrystal core increases in the soft ligand series **MAA** > **CYS** > **GSH**, with mercaptoacetic acid

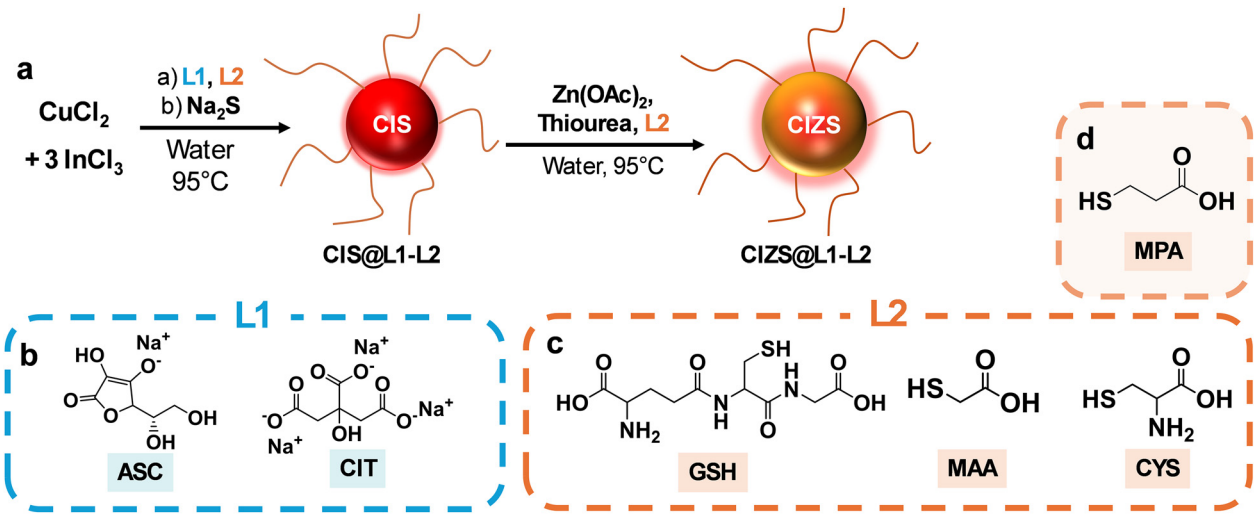

Fig. 1 Schematic representation of **CIZS@L1–L2** synthesis (a) and chemical structures of ligands **L1** and **L2** (b)–(d) used in this work.

Table 1 Structural and luminescence properties of **CIZS@L1–L2** in air-equilibrated aqueous solution at room temperature

	d_{TEM}[a]/nm	Cu : In : Zn[b]	E_{em}/eV	PLQY/%	τ_{av}[c]/ns
CIZS@CIT-MAA	3.1 ± 1.4	37 : 38 : 25	1.7	18	245
CIZS@ASC-MAA	3.8 ± 1.1	43 : 45 : 12	1.6	20	271
CIZS@CIT-CYS	3.6 ± 1.2	38 : 26 : 36	1.9	12	261
CIZS@ASC-CYS	4.1 ± 1.8	36 : 40 : 24	1.8	20	229
CIZS@CIT-GSH	3.4 ± 0.9	17 : 34 : 49	2.0	18	243
CIZS@ASC-GSH	3.4 ± 1.4	30 : 45 : 25	1.8	17	252
CIS@CIT-GSH	—[d]	40 : 60 : 0	Not detected	—	—

[a] Values are reported with the corresponding standard deviation calculated for the dimensional distribution obtained by STEM analysis. [b] Expressed as molar ratio. [c] Calculated as $(A_1\tau_1 + A_2\tau_2)/(A_1 + A_2)$, where A_1 and A_2 are the pre-exponential factors. The emission decay is measured at the maximum emission wavelength and with λ_{exc} = 405 nm. [d] Aggregation of the nanocrystals prevented a reliable estimation of the nanocrystal dimension.

ensuring almost stoichiometric nanocrystals. To better understand the reason for this result, we performed an additional synthesis with 1-mercaptopropionic acid (Fig. 1, **MPA**) as the soft ligand. **MPA** has the same binding sites as **MAA** (–SH and –COOH) and the same carbon backbone (C3) as **CYS**, without displaying its additional $-NH_2$ coordinating group. **CIZS@CIT-MPA** shows very similar composition and photophysical properties to **CIZS@CIT-MAA**, both of them significantly different from those of **CIZS@CIT-CYS** (Fig. S11). This result suggests that the length of the carbon backbone and thus ligand sterics play a minor role, and the binding strength is the most influential factor in determining nanocrystal composition.

The hard ligand has a stronger effect on the zinc content of the nanocrystal, as evidenced from Fig. 2b, with **CIT** showing the highest percentage of zinc in the crystal lattice.

It is interesting to note that the elemental composition of a core-only sample of quantum dots (**CIS@CIT-GSH**, Cu : In = 1.5) shows a lower Cu : In ratio than the corresponding shelled sample (**CIZS@CIT-GSH**, Cu : In = 2.0, Table 1 and Table S1). This evidence suggests that the addition of shell precursors not only promotes the epitaxial growth of a ZnS protective layer but also induces cation exchange, yielding an alloyed structure with graded composition. This observation agrees with the EDX results discussed previously and is further supported by spectroscopic data, as discussed in more detail below.

Photophysical properties of the nanocrystals

The investigated **CIZS@L1–L2** show the characteristic photophysical behaviour of Cu–In–Zn–S quantum dots,[41,42] featuring an absorption tail between 500 and 700 nm and a broad emission band at lower energy (Fig. 2). The emission intensity decays can be fitted with a biexponential function, and the average lifetime is of the order of 10^2 ns, with no significant variation as a function of the employed ligands (Table 1, Fig. S12). All **CIZS@L1–L2** show similar PLQY values, ranging from 0.12 (**CIZS@CIT-CYS**) to 0.20 (**CIZS@CIT-MAA**, Table 1).

On top of the above-discussed photophysical properties common to all the investigated samples, a closer look at the luminescence properties shows that the emission energy is deeply affected by the **L1–L2** couple employed during synthesis, spanning from 2.0 eV (**CIZS@CIT-GSH**) to 1.6 eV (**CIZS@ASC-MAA**). This result cannot be interpreted as a direct effect of the ligands on the optical properties of the nanocrystals, but rather as the effect of the ligands on the elemental composition of the nanocrystalline core (Fig. 2): a higher copper(I) content results in a red-shifted emission peak.[41,43]

Metal complex precursors in the synthesis of CIZS@L1–L2

To have a better understanding of the interaction between the soft ligands and the metal ions present in the nanocrystals, we performed spectrophotometric studies of the metal precursors with all the ligands analysed in this work. Fig. 3 shows the absorption and emission spectra acquired for the couple **CIT-GSH**, while the results obtained for other **L1–L2** couples are reported in the SI (Fig. S16), together with the spectra of all the isolated compounds.

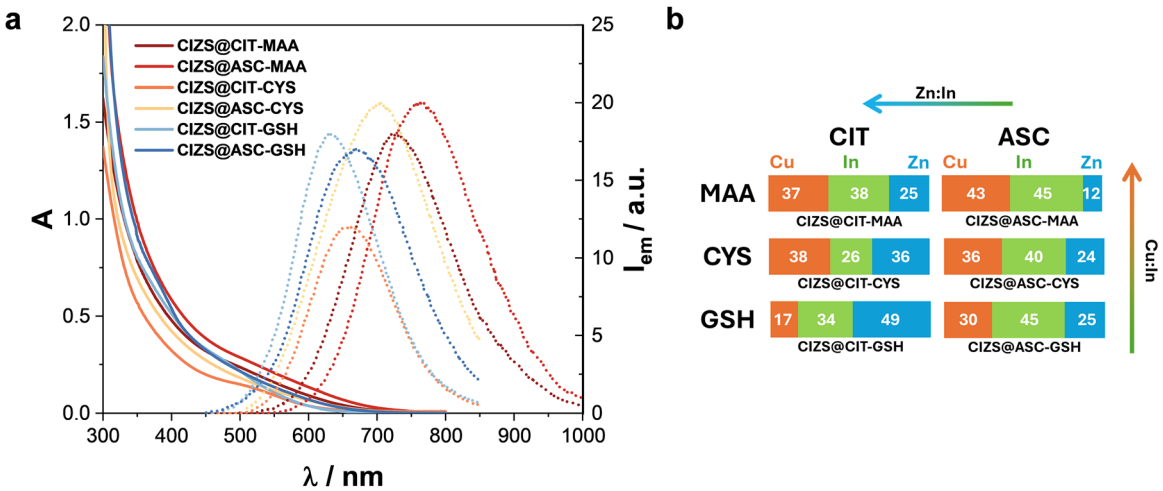

Fig. 2 (a) Absorption (solid lines) and emission spectra (dotted lines) of **CIZS@L1–L2** samples in air-equilibrated aqueous solution. λ_{exc} = 350 nm. Emission peaks are scaled according to PLQY. (b) Molar ratio of metal ions of **CIZS@L1–L2** samples determined by MP-AES analysis.

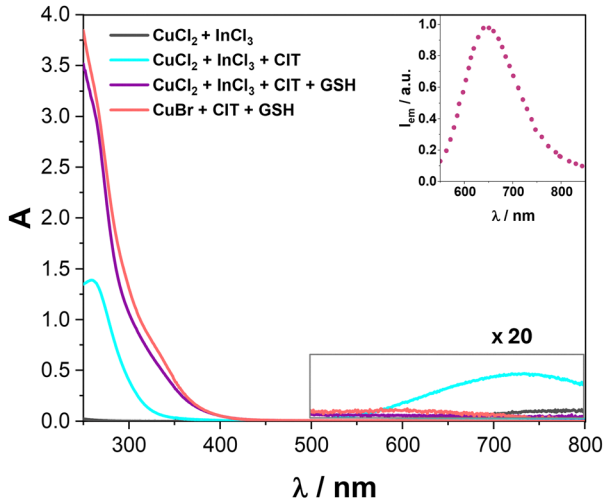

Fig. 3 Absorption (solid lines) spectra of a solution of $CuCl_2$ (0.6 mM) and $InCl_3$ (2 mM) in water upon addition of **CIT** and **GSH** with the same molar ratio as those used in synthesis (Cu : CIT : GSH = 1 : 10 : 20). Inset: emission of the solution after addition of **GSH** (λ_{exc} = 350 nm).

Upon addition of citrate to the metal precursors (Cu^{2+}, In^{3+} in water), two absorption bands centered at 260 nm and 740 nm appear (Fig. 3): they are ascribed to the formation of the **CuCIT2** complex, based on literature reports.[44] Upon addition of the thiolated soft ligands (**MAA**, **GSH** and **CYS**), the characteristic band of **CuCIT2** at 740 nm disappears, while two broad bands centered at 265 nm and 340 nm appear (Fig. S15).‡ A closely matching absorption spectrum is observed upon mixing Cu(I) bromide, **CIT** and a soft ligand in the same molar ratio in water (Fig. 3). Therefore, we attribute the disappearance of the absorption band peaked at 740 nm to the reduction of Cu(II) to Cu(I) by the thiolated ligands. Upon excitation of the solution at 350 nm a red emission is observed (the position of the peak depends on the thiolated ligand employed, see Fig. 3 for **GSH** and SI for **MAA** and **CYS**). Similar behaviour is obtained for the solution containing CuBr and **GSH**, while the same emission is not detected for a solution containing CuBr and **CIT** (Fig. S17). This demonstrates that the thiolated ligand not only reduces Cu(II) to Cu(I), but also modifies the coordination sphere of the metal complex. The luminescent band is reminiscent of that observed for Cu-thiolate nanoclusters.[45–48] It should be noted that all thiolated ligands exhibit similarly low reduction potentials (approximately −0.2 V *vs.* SHE),[49,50] compatible with Cu(II) reduction. This suggests that the reduction potential is not a determining factor in the formation of the Cu-thiolate nanoclusters or the resulting QDs.

When **CIT** is replaced by **ASC**, similar UV-Vis spectra are observed with minor differences, most probably due to the different pH value of the solution (Fig. S16).

On the other hand, the thiolated ligand employed (**GSH**, **MAA** or **CYS**) has a strong impact on the solubility in water and on the luminescent properties of the obtained Cu-thiolated clusters. This observation may indicate that the clusters serve as a precursor for the synthesis of QDs, determining the stoichiometry of the resulting QDs.

This possibility has already been reported for more conventional quantum dots,[51–56] but it has not been demonstrated for the synthesis of CIZS quantum dots in water. While a detailed investigation of this phenomenon lies beyond the scope of the present work, further studies are currently underway to address it.

In situ spectroscopic analysis of the growth of CIZS@L1–L2

The absorption spectra acquired during the synthesis of **CIZS@CIT-GSH** (Fig. 4) show that the nucleation starts immediately after Na_2S addition: the first spectrum recorded within 1 minute after its addition already displays the characteristic CIS absorption profile. The absorption of **CIZS@CIT-GSH** at the excitonic shoulder rapidly increases during the first 5 minutes and it slows down after 10–15 minutes (Fig. S18). Interestingly, the injection of the Zn^{2+} precursor solution causes an abrupt blue-shift in the absorption profile of the QDs. This supports the previous hypothesis that cation exchange occurs, and it indicates that Zn^{2+} rapidly diffuses in the nanocrystalline core. The incorporation of Zn^{2+} in the lattice leads to an increased band-gap, as previously reported.[40]

Repeating the same experiment in a fluorometer, the previously discussed red emission of the clusters (Fig. 4, gray dashed line) disappears right after the addition of Na_2S and no emission is detected during the growth of the **CIS@CIT-GSH** core. Zn^{2+} injection determines: (i) the appearance of an emission band peaked at 650 nm and (ii) an increase in emission intensity, suggesting that Zn^{2+} not only diffuses in the nanocrystalline core, but also forms an external ZnS protecting layer, increasing the PLQY of the resulting quantum dot. Altogether, both spectroscopic and structural analyses suggest that the synthetic conditions employed in this work promote an initial rapid cation exchange (Cu^{+} for Zn^{2+}), followed by the growth of a ZnS shell. The resulting structure is likely an alloyed core–shell system, characterized not by a distinct core–shell boundary but by a

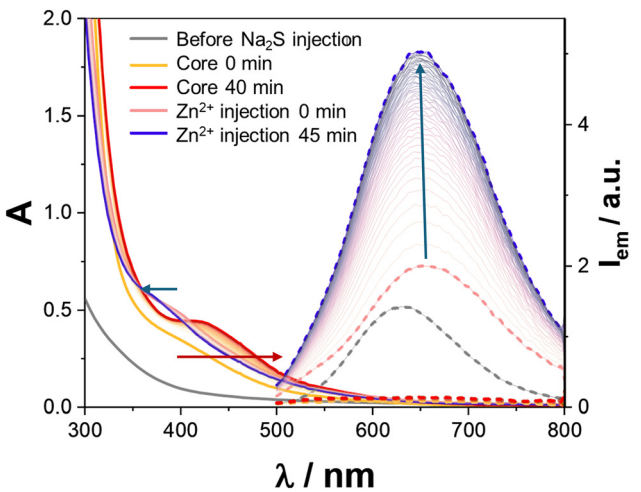

Fig. 4 Absorption (solid lines) and emission spectra (dotted lines) acquired during the air-equilibrated synthesis of **CIZS@CIT-GSH** in water at 70 °C. The red and blue arrows indicate the trend of the spectra recorded before and after Zn^{2+} injection, respectively. Spectra are acquired for 1 minute and the concentration of the precursors is reduced to one-fourth of that used during synthesis to remain within the spectrophotometer detection limit.

graded interface with mixed composition. This interpretation is in agreement with a reported investigation on the $CuInS_2$/ZnS system,[40] which shows that low temperatures (<150 °C) favor cation substitution and alloying in heating-up synthesis in organic solvents.

The other **CIZS@L1–L2** show similar results, confirming that in all cases QD growth is extremely fast due to the high reactivity of Na_2S and that all ligands result in an alloyed core–shell structure (Fig. S19–S23). For some of the batches a weak emission is observed also for the **CIS@L1–L2** core (Fig. S19–S23) and Zn^{2+} injection causes a blue-shift and an increase in the emission intensity.

Stability of CIZS@L1–L2

The different ligands employed in the synthesis confer different stabilities to CIZS quantum dots in aqueous solution, as demonstrated by the time-evolution of PLQY (Fig. 5). The soft ligand has the strongest effect. **MAA** and **GSH** are the best soft ligands, ensuring high PLQY and full retention of the photophysical properties for several weeks. In addition to that, both these ligands allow the storage of quantum dots as a powder (after precipitation and drying) with no significant change in the photophysical properties once the QDs are re-dispersed in water: this is very convenient for practical uses. On the other hand, when **CYS** is employed, degradation of the QDs and concomitant formation of a green-emitting species are observed (Fig. S26 and S27) within 2–5 days. The luminescent byproduct shows a broad and featureless absorption spectrum, together with an excitation-dependent emission (Fig. S30). This is likely due to the catalytic oxidation of thiolated molecules promoted by Cu^+ ions, which leads to the formation of luminescent carbon dots, already reported in the literature.[57] The process strips copper ions from the QDs' surface and eventually dissolves them. As a further proof of this mechanism, TEM analysis on degraded samples shows that, as opposed to fresh samples, copper and indium are no longer co-localised, but they are present in different phases identified as CuS and an indium- and oxygen-rich compound (Fig. S31). The QD degradation liberates Cu^+ and In^{3+} ions in solution that react with oxygen (In^{3+}) and residual sulphur (Cu^+) to form the aforementioned phases.

Both **CIZS@ASC-CYS** and **CIZS@CIT-CYS** show the same degradation mechanism, although **ASC** slightly slows down the dissolution reaction.

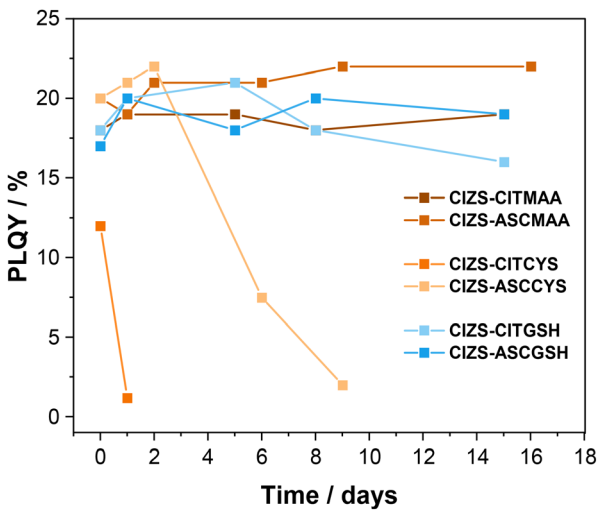

Fig. 5 PLQY stability of **CIZS-L1–L2** in air-equilibrated water solution over time.

Conclusions

This work demonstrates the critical role of the ligands in directing the synthesis of CIZS quantum dots in water. We showed that thiolated ligands are essential for achieving high PLQY in water (~20%) and excellent colloidal stability, while non-thiolated ligands result in poorly emissive and unstable nanocrystals.

Notably, ligand identity – and more specifically binding strength – governs emission energy by controlling the metal ion composition of the nanocrystals in terms of Cu : In : Zn molar ratio. Furthermore, EDX mapping indicates that this synthesis produces alloyed nanoparticles with a graded composition. Copper and indium are predominantly localized in the central region of the nanoparticles, while zinc is distributed more homogeneously throughout the entire volume.

In situ optical measurements demonstrate the formation of emissive copper clusters prior to Na_2S injection, suggesting their involvement as precursors in the nucleation and growth of CIZS nanocrystals – a mechanism that opens new avenues for reaction pathway control. After the injection of the sulphur precursor, the kinetic evolution of the absorption and emission spectra shows a rapid growth of the quantum dot core. A blue-shift of the lowest energy absorption band and a strong increase of PLQY are observed after Zn^{2+} addition, suggesting that the employed water-based route favours the generation of alloyed core–shell architectures. Together, these insights provide a foundation for the rational design of green, water-based synthetic strategies for high-performance quantum dots.

Experimental section

Materials

$CuCl_2$ (98%), $InCl_3$ (99%), $Zn(AcO)_2$ (99%), Na_2S (≥90%), NaOH (98%), HNO_3 (65%), HCl (37%), L-glutathione reduced (GSH, 99%), L-cysteine (CYS, 99%), mercaptoacetic acid (MAA, 99%), sodium citrate dihydrate (99%), sodium ascorbate (99%) and thiourea (99%) were purchased from Sigma-Aldrich and used with no additional purification. Water was deionized by reverse osmometry with an Elga Purelab Classic purification system (13 MΩ cm). Acetone (ACS) was purchased by Sigma-Aldrich and used with no further purification.

Synthesis of **CIZS@L1–L2**: the synthesis of the quantum dots was performed in closed vessels heated with a heating plate equipped with a thermocouple to control the temperature. The following stock solutions were prepared: $CuCl_2$ 0.013M in water, $InCl_3$ 0.25 M in ethanol, L1 (**NaCIT** or **NaASC**) 0.4 M in water, Na_2S 1 M in water and, for the second step of the

synthesis (Fig. 1), a solution (named hereafter "shell solution") containing $Zn(OAc)_2$ 0.04 M, $SC(NH_2)_2$ 0.03 M, and **L2** (**GSH**, **CYS** or **MAA**) 0.2 M in water. The pH of the latter solution is adjusted to 6.5–7 by addition of a few drops of NaOH 1 M, which also allows the complete dissolution of a cloudy white precipitate that is initially formed. In a typical synthesis, 600 μL of $CuCl_2$ (6 μmol, 1 eq.) stock solution is added to 10 mL of deionized water, together with 80 μL of $InCl_3$ (20 μmol, 3 eq.) stock solution. Subsequently, 200 μL of **L1** (80 μmol, 13 eq.) stock solution and 120 μmol (20 eq.) of **L2** are added to the solution. After that, 96 μL of Na_2S (96 μM, 16 eq.) stock solution is added to the solution and the reaction vessel is stirred in a pre-heated bath at 95 °C for 40 minutes. Subsequently, 3 mL of the shell solution is added under stirring and the reaction mixture is stirred at 95 °C for an additional 45 minutes. The nanocrystal growth is stopped upon cooling of the reaction vessels in a cold-water bath. The batches are stored in bidistilled water at room temperature.

Material characterisation

The elemental composition of **CIZS@L1–L2** was determined *via* an Agilent 4210 MP-AES atomic emission spectrometer. For this purpose, the batches are precipitated once in acetone and then redispersed in water. The pH of these solutions is adjusted to 3 to obtain full precipitation of **CIZS@L1–L2**. The dispersion is centrifuged, and the precipitate is dissolved in 3 mL HNO_3 7 M. In 1–3 days, these solutions are completely transparent and homogeneous, indicating full digestion of the nanocrystals.

Powder XRD measurements were performed on a Panalytical X'Pert pro powder diffractometer equipped with a Cu X-Ray tube (Kα radiation, 1.54184 Å, 40 mA, 40 kV), with a Bragg–Brentano configuration and X'celerator detector. For acquiring the diffraction pattern of a sample, a suspension of **CIZS@L1–L2** in water is precipitated in acetone, centrifuged and the resulting powder is dried overnight under a rotative pump. The dried powder is then deposited on a zero-background silicon sample holder and a continuous scan from 15° to 60 °C is performed with an acquisition time of 15 minutes.

High angle annular dark field (HAADF)-STEM micrographs were recorded *via* an FEI Tecnai F20T TEM equipped with a 200 kV Schottky emitter. The TEM was equipped with an MSC794 Gatan CCD camera, a Fischione HAADF-STEM detector, and a double tilt sample holder. The samples were purified once *via* precipitation in an antisolvent (acetone) to avoid excessive amounts of free ligands in the sample. The purified solutions were deposited by drop casting on an Au TEM grid with a lacey ultrathin continuous carbon film. Water was evaporated at 80 °C overnight on a hot plate. Evaluation of the average diameter was performed by taking into account high magnification images, analysing nanoparticles for each sample from several images. In total, around 100 nanoparticles per sample were evaluated, considering the ones with spherical morphology, due to the presence of some aggregates. All fittings were made using a Gaussian equation (3 parameters).

High resolution STEM (HRSTEM) HAADF images were acquired on a probe-corrected Thermo Fisher Spectra 300 S/TEM operated at 300 kV. Compositional maps were obtained using a Dual-X EDX detector configuration with a total acquisition solid angle of 1.74 sr. The EDX signal was processed using Velox.

Photophysical characterisation

Photophysical measurements were performed in air-equilibrated bidistilled water at room temperature, unless otherwise noted. The batches were not purified before photophysical characterisation, as precipitation in antisolvents (acetone or isopropanol) rendered **CIZS@CIT-CYS** and **CIZS@ASC-CYS** indispersible in any solvent. The addition of cysteine to the samples does not improve their dispersibility. To obtain suitable concentrations, **CIZS@L1–L2** samples were diluted 1 : 4 after synthesis. UV-visible absorption spectra were recorded with a PerkinElmer λ_{650} spectrophotometer, using quartz cells with a 1.0 cm path length. Emission spectra were obtained with an Edinburgh FS5 with a PMT980 and an InGaAs detector for the visible and NIR spectral range, respectively. Correction of the emission spectra for detector sensitivity in the 550–1000 nm spectral region was performed by a calibrated lamp.[58] PLQY were measured following the method of Demas and Crosby[59] (standard used: $[Ru(bpy)_3]^{2+}$ in air equilibrated aqueous solution Φ = 0.0407). PL lifetime measurements were performed by an Edinburgh FLS920 spectrofluorometer equipped with a TCC900 card for data acquisition in time-correlated single photon counting experiments (0.2 ns time resolution) with a LDH–P–C–405 pulsed diode laser. For temperature-controlled experiments, the temperature of the cuvette was controlled *via* a Julabo F12 temperature controller unit directly connected to the spectrofluorometer or spectrophotometer cuvette holder. The estimated experimental errors are: 2 nm on the band maxima, 15% on the molar absorption coefficient and luminescence lifetime, and 10% on the PLQY.

Author contributions

The manuscript was written through contributions of all authors. All authors have given approval to the final version of the manuscript.

Conflicts of interest

There are no conflicts to declare.

Data availability

The data that support the findings of this study are available from the corresponding author upon reasonable request.

Supplementary information (SI): SI includes structural characterisation (XRD, TEM, STEM-EDX) and additional spectroscopic data. See DOI: https://doi.org/10.1039/d5nh00817d.

Acknowledgements

The project PRIDE (Produzione sostenibile di idrogeno tramite sistemi disaccoppiati) funded by the MASE - grant F57G25000320006 – is gratefully acknowledged.

Notes and references

‡ It should be noted that the previously discussed bands cannot be attributed to any of the free ligands, as GSH and CIT do not exhibit significant absorption at $\lambda > 250$ nm (Fig. S15).

1 H. Shen, Q. Gao, Y. Zhang, Y. Lin, Q. Lin, Z. Li, L. Chen, Z. Zeng, X. Li, Y. Jia, S. Wang, Z. Du, L. S. Li and Z. Zhang, *Nat. Photonics*, 2019, **13**, 192–197.
2 S. Zhou, Y. Ma, X. Zhang, W. Lan, X. Yu, B. Xie, K. Wang and X. Luo, *ACS Appl. Nano Mater.*, 2020, **3**, 814–819.
3 A. Zebibula, N. Alifu, L. Xia, C. Sun, X. Yu, D. Xue, L. Liu, G. Li and J. Qian, *Adv. Funct. Mater.*, 2018, **28**, 1703451.
4 P. Roy, M. Virmani and P. P. Pillai, *Chem. Sci.*, 2023, **14**, 5167–5176.
5 L. C. Spangler, R. Chu, L. Lu, C. J. Kiely, B. W. Berger and S. McIntosh, *Nanoscale*, 2017, **9**, 9340–9351.
6 O. T. Bruns, T. S. Bischof, D. K. Harris, D. Franke, Y. Shi, L. Riedemann, A. Bartelt, F. B. Jaworski, J. A. Carr, C. J. Rowlands, M. W. B. Wilson, O. Chen, H. Wei, G. W. Hwang, D. M. Montana, I. Coropceanu, O. B. Achorn, J. Kloepper, J. Heeren, P. T. C. So, D. Fukumura, K. F. Jensen, R. K. Jain and M. G. Bawendi, *Nat. Biomed. Eng.*, 2017, **1**, 0056.
7 A. Hassan, J. Kaur, O. Chen and M. G. Bawendi, *MRS Bull.*, 2025, **50**, 1–15.
8 G. Morselli, M. Villa, A. Fermi, K. Critchley and P. Ceroni, *Nanoscale Horiz.*, 2021, **6**, 676–695.
9 B. Harrington, Z. Ye, L. Signor and A. D. Pickel, *ACS Nanosci. Au*, 2024, **4**, 30–61.
10 M. Booth, A. P. Brown, S. D. Evans and K. Critchley, *Chem. Mater.*, 2012, **24**, 2064–2070.
11 L. Li, A. Pandey, D. J. Werder, B. P. Khanal, J. M. Pietryga and V. I. Klimov, *J. Am. Chem. Soc.*, 2011, **133**, 1176–1179.
12 A. A. Abdellatif, M. A. Younis, M. Alsharidah, O. A. Rugaie and H. M. Tawfeek, *Int. J. Nanomed.*, 2022, **17**, 1951–1970.
13 K. J. McHugh, L. Jing, A. M. Behrens, S. Jayawardena, W. Tang, M. Gao, R. Langer and A. Jaklenec, *Adv. Mater.*, 2018, **30**, 1706356.
14 Nobel Prize in Chemistry 2023, https://www.nobelprize.org/prizes/chemistry/2023/advanced-information/, (accessed December 15, 2025).
15 E. Oh, R. Liu, A. Nel, K. B. Gemill, M. Bilal, Y. Cohen and I. L. Medintz, *Nat. Nanotechnol.*, 2016, **11**, 479–486.
16 Y. Wang, R. Hu, G. Lin, I. Roy and K.-T. Yong, *ACS Appl. Mater. Interfaces*, 2013, **5**, 2786–2799.
17 Q. Xu, J. Gao, S. Wang, Y. Wang, D. Liu and J. Wang, *J. Mater. Chem. B*, 2021, **9**, 5765–5779.
18 M. Zhang, B. P. Bishop, N. L. Thompson, K. Hildahl, B. Dang, O. Mironchuk, N. Chen, R. Aoki, V. C. Holmberg and E. Nance, *Nanoscale Adv.*, 2019, **1**, 3424–3442.
19 X. Long, X. Tan, Y. He and G. Zou, *J. Mater. Chem. C*, 2017, **5**, 12393–12399.
20 E. S. Speranskaya, C. Sevrin, S. De Saeger, Z. Hens, I. Y. Goryacheva and C. Grandfils, *ACS Appl. Mater. Interfaces*, 2016, **8**, 7613–7622.
21 R. Marin, A. Vivian, A. Skripka, A. Migliori, V. Morandi, F. Enrichi, F. Vetrone, P. Ceroni, C. Aprile and P. Canton, *ACS Appl. Nano Mater.*, 2019, **2**, 2426–2436.
22 C.-W. Chen, D.-Y. Wu, Y.-C. Chan, C. C. Lin, P.-H. Chung, M. Hsiao and R.-S. Liu, *J. Phys. Chem. C*, 2015, **119**, 2852–2860.
23 M. Villa, S. Angeloni, A. Bianco, A. Gradone, V. Morandi and P. Ceroni, *Nanoscale*, 2021, **13**, 12460–12465.
24 Z. Ziani, C. Bellatreccia, F. P. Battaglia, G. Morselli, A. Gradone, P. Ceroni and M. Villa, *Nanoscale*, 2024, 12947–12956.
25 C. Wang, X. Tong, W. Wang, J.-Y. Xu, L. V. Besteiro, A. I. Channa, F. Lin, J. Wu, Q. Wang, A. O. Govorov, A. Vomiero and Z. M. Wang, *ACS Appl. Mater. Interfaces*, 2020, **12**, 36277–36286.
26 K. Y. Zhang, Q. Yu, H. Wei, S. Liu, Q. Zhao and W. Huang, *Chem. Rev.*, 2018, **118**, 1770–1839.
27 N. Tsolekile, S. Nahle, N. Zikalala, S. Parani, E. H. M. Sakho, O. Joubert, M. C. Matoetoe, S. P. Songca and O. S. Oluwafemi, *Sci. Rep.*, 2020, **10**, 4936.
28 C. Bellatreccia, Z. Ziani, A. Germinario, S. Engelaar, F. P. Battaglia, A. Gradone, M. Villa and P. Ceroni, *Small*, 2024, **20**, 2404425.
29 A. D. P. Leach and J. E. Macdonald, *J. Phys. Chem. Lett.*, 2016, **7**, 572–583.
30 R. Marin and D. Jaque, *Chem. Rev.*, 2021, **121**, 1425–1462.
31 Y. Chen, S. Li, L. Huang and D. Pan, *Inorg. Chem.*, 2013, **52**, 7819–7821.
32 L. Branzi, F. Purcell-Milton, C. Cressoni, M. Back, E. Cattaruzza, A. Speghini, Y. K. Gun'ko and A. Benedetti, *Nanoscale*, 2022, **14**, 12174–12182.
33 M. A. Abate, K. Dehvari, J.-Y. Chang and K. Waki, *Dalton Trans.*, 2019, **48**, 16115–16122.
34 J. Lee and C.-S. Han, *Nanoscale Res. Lett.*, 2015, **10**, 145.
35 C. Zhao, Z. Bai, X. Liu, Y. Zhang, B. Zou and H. Zhong, *ACS Appl. Mater. Interfaces*, 2015, **7**, 17623–17629.
36 R. Marin, A. Skripka, L. V. Besteiro, A. Benayas, Z. Wang, A. O. Govorov, P. Canton and F. Vetrone, *Small*, 2018, **14**, 1803282.
37 S. Zang, X. Zhang, Y. Sun, N. Li, L. Wang and L. S. Li, *Front. Chem.*, 2022, **10**, 1102514.
38 K. Gugula, L. Stegemann, P. J. Cywiński, C. A. Strassert and M. Bredol, *RSC Adv.*, 2016, **6**, 10086–10093.
39 J. Choi, W. Choi and D. Y. Jeon, *ACS Appl. Nano Mater.*, 2019, **2**, 5504–5511.
40 A. C. Berends, W. van der Stam, J. P. Hofmann, E. Bladt, J. D. Meeldijk, S. Bals and C. de Mello Donega, *Chem. Mater.*, 2018, **30**, 2400–2413.
41 G. Zaiats, S. Kinge and P. V. Kamat, *J. Phys. Chem. C*, 2016, **120**, 10641–10646.
42 G. Morselli, C. Bellatreccia, M. Mazzanti, V. Cristino, A. Ianniello, S. Caramori, R. Mazzaro and P. Ceroni, *Adv. Opt. Mater.*, 2024, **12**, 2400259.
43 D. H. Jara, K. G. Stamplecoskie and P. V. Kamat, *J. Phys. Chem. Lett.*, 2016, **7**, 1452–1459.
44 E. R. Still and P. Wikberg, *Inorg. Chim. Acta*, 1980, **46**, 147–152.
45 M. T. Morgan, L. A. H. Nguyen, H. L. Hancock and C. J. Fahrni, *J. Biol. Chem.*, 2017, **292**, 21558–21567.
46 B. K. Maiti, K. Pal and S. Sarkar, *Eur. J. Inorg. Chem.*, 2007, 5548–5555.

47 K. Fujisawa, S. Imai, N. Kitajima and Y. Moro-oka, *Inorg. Chem.*, 1998, **37**, 168–169.
48 S. Huseyinova, J. M. B. Trillo, J. M. Ramallo-López, F. G. Requejo, D. Buceta and M. Arturo López-Quintela, *Phys. Chem. Chem. Phys.*, 2023, **25**, 6025–6031.
49 P. C. Jocelyn, *Eur. J. Biochem.*, 1967, **2**, 327–331.
50 *Handbook of Biochemistry and Molecular Biology*, ed. R. Lundblad and F. Macdonald, CRC Press, Boca Raton, 4th edn, 2010.
51 B. Santiago-González, A. Monguzzi, V. Pinchetti, A. Casu, M. Prato, R. Lorenzi, M. Campione, N. Chiodini, C. Santambrogio, F. Meinardi, L. Manna and S. Brovelli, *ACS Nano*, 2017, **11**, 6233–6242.
52 S. F. Sandeno, K. J. Schnitzenbaumer, S. M. Krajewski, R. A. Beck, D. M. Ladd, K. R. Levine, D. Dayton, M. F. Toney, W. Kaminsky, X. Li and B. M. Cossairt, *J. Am. Chem. Soc.*, 2024, **146**, 3102–3113.
53 J. Zhang, X. Hao, N. Rowell, T. Kreouzis, S. Han, H. Fan, C. Zhang, C. Hu, M. Zhang and K. Yu, *J. Phys. Chem. Lett.*, 2018, **9**, 3660–3666.
54 S. J. Shin, J.-J. Koo, J.-K. Lee and T. D. Chung, *Sci. Rep.*, 2019, **9**, 20144.
55 S. L. Cumberland, K. M. Hanif, A. Javier, G. A. Khitrov, G. F. Strouse, S. M. Woessner and C. S. Yun, *Chem. Mater.*, 2002, **14**, 1576–1584.
56 Z. Li, W. Cai and J. Sui, *Nanotechnology*, 2007, **19**, 035602.
57 L. Branzi, G. Lucchini, E. Cattaruzza, N. Pinna, A. Benedetti and A. Speghini, *Nanoscale*, 2021, **13**, 10478–10489.
58 M. Montalti, A. Credi, L. Prodi, M. T. Gandolfi, J. Michl and V. Balzani, *Handbook of photochemistry*, CRC/Taylor & Francis, Boca Raton, 3rd edn, 2020.
59 K. Suzuki, A. Kobayashi, S. Kaneko, K. Takehira, T. Yoshihara, H. Ishida, Y. Shiina, S. Oishi and S. Tobita, *Phys. Chem. Chem. Phys.*, 2009, **11**, 9850.

